Oxygen-induced nano-faceting of Ir(210)

5 AUTHORS, INCLUDING:

Wenhua Chen
Rutgers, The State University of New J…

43 PUBLICATIONS **186** CITATIONS

SEE PROFILE

Jamie S Quinton
Flinders University

96 PUBLICATIONS **911** CITATIONS

SEE PROFILE

Oxygen-induced nano-faceting of Ir(2 1 0)

Ivan Ermanoski, Kalman Pelhos, Wenhua Chen, Jamie S. Quinton,
Theodore E. Madey *

*Department of Physics and Astronomy and Laboratory for Surface Modification, Rutgers—The State University of New Jersey,
136 Frelinghuysen Road, Piscataway, NJ 08854-8019, USA*

Abstract

The adsorption of oxygen and the nanometer-scale faceting induced by oxygen have been studied on Ir(2 1 0). Oxygen is found to chemisorb dissociatively on Ir(2 1 0) at room temperature. The molecular desorption process is complex, as revealed by a detailed kinetic analysis of desorption spectra. Pyramid-shaped facets with {3 1 1} and (1 1 0) orientations are formed on the oxygen-covered Ir(2 1 0) surface when annealed to $T \geqslant 600$ K. The surface remains faceted for substrate temperatures $T < 850$ K. For $T > 850$ K, the substrate structure reverts to the oxygen-covered (2 1 0) planar state and does so reversibly, provided that oxygen is not lost due to desorption or via chemical reactions upon which the planar (2 1 0) structure remains. A clean faceted surface was prepared through the use of low temperature surface cleaning methods: using CO oxidation, or reaction of H_2 to form H_2O, oxygen can be removed from the surface while preserving ("freezing") the faceted structure. The resulting clean faceted surface remains stable for $T < 600$ K. For temperatures above this value, the surface irreversibly relaxes to the planar state.
© 2003 Published by Elsevier B.V.

Keywords: Faceting; Iridium; Oxygen; Chemisorption; Thermal desorption; Low energy electron diffraction (LEED); Auger electron spectroscopy

1. Introduction

Atomically rough clean metal surfaces generally have lower surface atom density and higher surface free energy than close-packed surfaces of the same metal. Nonetheless, such surfaces can be prepared as stable orientations, e.g. body-centered cubic (bcc) Mo(1 1 1), W(1 1 1); and face-centered cubic (fcc) Pt(2 1 0), Ir(2 1 0), etc. The presence of adsorbates, especially those that interact strongly with the substrate, can cause changes in surface morphology through mechanisms such as reconstruction and facet formation [1–9]. These morphological changes are usually explained in terms of changes in surface free energy due to the presence of adsorbate [10,11]. There are many overlayer/substrate systems that exhibit faceting, including oxygen and metal covered W(1 1 1) and Mo(1 1 1) [4–6]; gas covered Cu(2 1 0), Ni(2 1 0) and Pt(2 1 0) [2,3,7]; and gas covered vicinal Cu surfaces [8,9]. It has been observed that changes in morphology can be accompanied by changes in electronic structure and surface reactivity [12,13].

---

* Corresponding author. Tel.: +1-732-445-5185; fax: +1-732-445-4991.

E-mail address: madey@physics.rutgers.edu (T.E. Madey).

The most thoroughly studied substrate to date, the bcc W(1 1 1) surface, exhibits faceting upon annealing to $T > 800$ K when covered with single atomic layers of Pt, Pd, Rh, Ir, Au, Ru, O and Cl [12,14,15]. The phenomenon of faceting has also been interpreted using first principles local density (LDA) calculations, giving insight into the surface free energy and kinetic conditions that make facet formation possible [10,16]. Evidence for structure sensitivity in the surface chemistry of acetylene and in butane hydrogenolysis has been observed over Pt/W and Pd/W faceted surfaces [17,18]. The surface electronic properties of metal thin films on W(1 1 1) have also been studied in detail [19].

As part of our ongoing project to study the morphological stability of atomically rough metal surfaces, we extend our previous work on surfaces such as W(1 1 1), W(2 1 1) and Mo(1 1 1), to Ir(2 1 0). Previous studies on fcc (2 1 0) surfaces indicate that facet formation is induced by oxygen and activated nitrogen on Cu(2 1 0) and Ni(2 1 0) [2,3], while oxygen adsorption and CO catalytic oxidation induce faceting on Pt(2 1 0) [7]. Iridium is an fcc metal of the platinum group with melting point $T_m = 2739$ K and an ideal model of its surface is illustrated in Fig. 1. The bulk truncation of this surface is atomically very open and rough, with four exposed layers of atoms. The top layer has C_{2v}

Fig. 1. Hard sphere model of an fcc (2 1 0) surface.

symmetry (180° rotation, with the [2 1 0] vector as the z-axis and principal axis, as well as one vertical reflection plane defined by the [2 1 0] and [$\bar{1}$ 2 0] vectors). The bulk crystal has reduced symmetry: the same vertical reflection plane and no axis of rotational symmetry. The z-periodicity of the structure is 10 layers—the atoms of the 11th layer are in the same x and y positions as the atoms in the top layer and 0.91 nm below it. The motivation to extend our experiments to a platinum group fcc metal stems in part from interest in the rich catalytic properties that these materials exhibit and their widespread use in catalytic applications.

In this paper we present the results of temperature programmed desorption (TPD), low energy electron diffraction (LEED) and Auger electron spectroscopy (AES) experiments involving oxygen adsorption on the Ir(2 1 0) surface, and the oxygen-induced faceting of Ir(2 1 0) that occurs upon annealing. The TPD experimental results and a brief analysis of the desorption spectra are presented in Section 3.1. Results concerning the facet formation on the oxygen-covered surface, and facet properties are in Sections 3.2–3.5. A very important aspect of iridium faceting—preparation and properties of a clean faceted surface—is described in Section 3.6. Further analysis and interpretation of all of the results are discussed in Section 4. Details of the desorption spectra analysis are in Appendix A.

2. Experimental

The experiments were carried out in a stainless steel ultrahigh vacuum (UHV) system pumped by a combination of turbomolecular, ion, and titanium sublimation pumps to a base pressure of 1×10^{-10} Torr, measured with an uncalibrated commercial Bayard-Alpert type ionization gauge. A number of surface diagnostic techniques were used, including LEED, AES and TPD spectroscopy. The LEED optics are of the front view type, with four grids and an acceptance angle of 120°, and the sample was always oriented perpendicular to the incident electron beam during LEED measurements. A grazing incidence electron gun (typically operated at 3 keV incident electron energy)
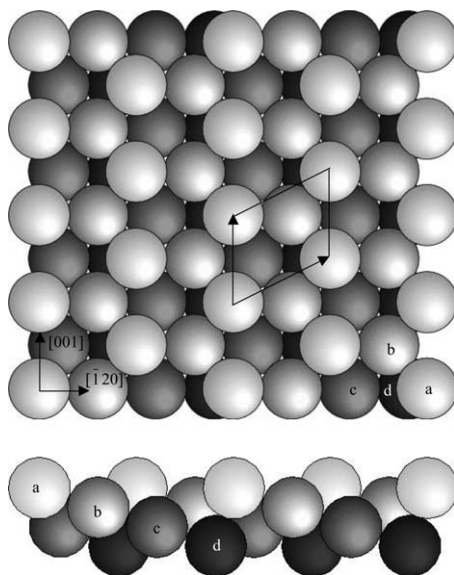
and a double pass cylindrical mirror analyzer are used for AES. For TPD and for residual gas analysis (RGA), a quadruple mass spectrometer (QMS) is employed.

The sample is cut from a single crystal Ir (99.99%) rod ∼10 mm in diameter, ∼1.5 mm thick, aligned within 0.5° of the (2 1 0) orientation and polished to a mirror finish. The sample support assembly is specially designed to permit a very wide sample temperature range (100–2500 K) while minimizing both outgassing during high temperature experiments and subsequent cooling times. The sample is supported by two leads made of rhenium foil (approximately $12 \times 3 \times 0.1$ mm^3) that are spotwelded directly to its rear side. Rhenium is a most suitable choice for this application because it has a very high melting point ($T_m = 3459$ K) and has no low melting point alloys with iridium [20]. The leads are also used for resistive heating by passing a high current (up to 45 A) through the leads and sample. Cooling is achieved by circulating chilled water. The experiments described in this work were performed at temperatures between 280 (lowest available by water cooling) and 2100 K (high temperature anneals). Accurate temperature measurement is achieved by using a C-type (W–5 at.% Re/W–26 at.% Re) thermocouple which is also spotwelded directly to the rear of the sample. Temperatures up to 1900 K can be attained by resistive heating, but for swift (2–3 s) high temperature flashes, electron bombardment is usually used. A spiral tungsten filament is mounted immediately (∼1–2 mm) behind the sample for this purpose. The typical voltage applied to the sample during these flashes is 1.5 kV, and the maximum output power is around 150 W, almost all of which is dissipated at the sample.

The surface is cleaned by repetitive electron bombardment anneals to ∼2000 K in O$_2$ at 10^{-7} Torr and subsequent rapid flashes to ∼2000 K in UHV. Heating to a very high temperature facilitates carbon diffusion to the surface where it is oxidized to CO which readily desorbs. Any oxygen remaining on the surface after the first part of the procedure is then desorbed during the flashes in UHV and cleanliness is verified by AES and TPD measurements. The only contaminant detected was carbon, in amounts that, after numerous cleaning cycles, were comparable to the noise level and therefore difficult to estimate, but are of the order of one percent of a monolayer or less.

Interestingly, resistively heating the sample was found to cause only a minor displacement and a barely noticeable distortion of the surface's LEED pattern. This makes it possible to perform LEED measurements and monitor pattern changes as a function of temperature up to $T \sim 900$ K. Both 35 mm film and digital cameras were used to record the patterns presented in this paper.

Gas deposition was achieved by back-filling the chamber. For oxygen (Matheson, research purity 99.998% O$_2$) deposition background pressures between 5×10^{-9} and 1×10^{-7} Torr were used, depending on the desired dose. The crystal was exposed to oxygen doses (D) ranging from 0.05 to 80 L (1 L = 10^{-6} Torr s, 1 Torr = 133 Pa) at room temperature. To obtain TPD spectra, the sample, which was positioned in front of a QMS, was resistively heated at a controlled rate. The QMS has a small aperture at its entrance, and the sample, which faces the aperture, is placed 2–3 mm in front of it. The heating rate was $\beta = 5$ K/s and was under computer control to ensure negligible deviations from linearity (the maximum random deviation from the target temperature was less than 0.1 K at all times).

Oxygen presence on the surface was detected by AES and TPD. Careful TPD measurements (recording the $m = 32$ amu signal) were performed for the entire range of oxygen exposures. Particular attention was paid to ensure identical initial experimental conditions (sample preparation and dosing) and detection efficiency for each measurement. The original TPD data were initially smoothed (the number of data points in a raw spectrum is 10^5, or about 100 points/K), and then a linear background was subtracted from each spectrum individually.

3. Results

3.1. Oxygen adsorption and desorption

TPD spectra for oxygen dosed onto Ir(2 1 0) at room temperature are shown in Fig. 2. For low
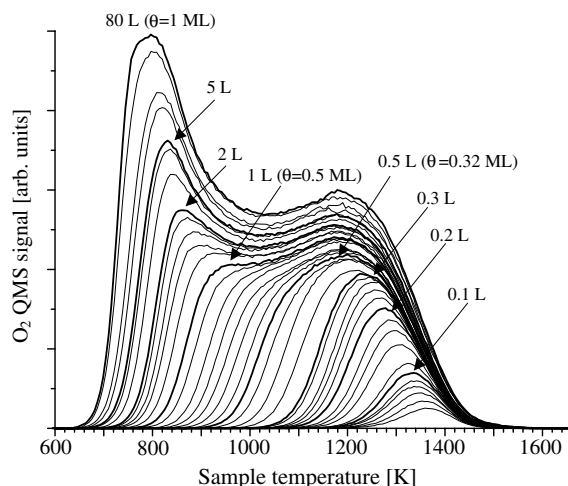
Fig. 2. TPD spectra of O/Ir(2 1 0). Deposition is performed at room temperature; linear heating rate is 5 K/s.

Fig. 3. TPD uptake curves for O/Ir(2 1 0). Circles: exposure range 0–5 L. Squares: exposure range 0–80 L. Inset (a): details of the uptake curve for low exposure. Inset (b): AES uptake curve.

oxygen coverage the peaks are symmetric, and the peak position steadily shifts to lower temperature as the dose increases. Furthermore, the curves have a common trailing edge, but the peak width increases with coverage. For doses above $D = 0.5$ L a shoulder develops on the low temperature side and as coverage increases, this feature becomes an additional, distinct peak. Based on the integrated area under the TPD spectra an uptake curve for the series of doses was obtained and is shown in Fig. 3. For low doses (inset (a)) most of the adsorption sites are unoccupied and the uptake curve is very close to linear. As the dose increases to tens of Langmuirs, the uptake curve approaches an asymptotic value. At this point the surface density of adsorbed oxygen atoms, n (atom/m^2), approaches a maximum (saturation) value n_s, and the coverage, defined as $\theta = n/n_s$, reaches $\theta_s = 1$ ML [1] [21]. This is in agreement with the similar, although not as accurate, uptake curve plotted by using AES peak intensities (inset (b)). The oxygen coverage for all doses quoted throughout this paper is calculated based on the integrated surface area under the corresponding TPD spectrum, and
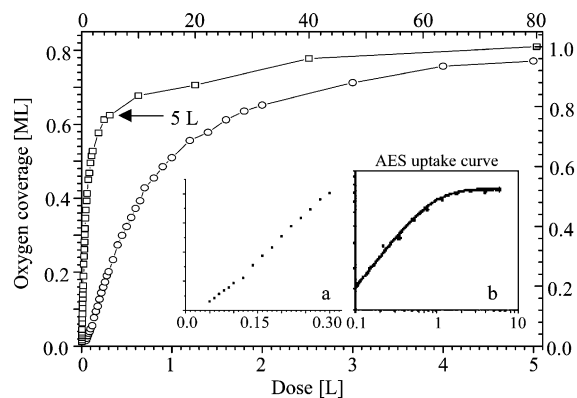
ranges between 0.015 and 1 ML. Note also that extrapolating to very low doses indicates no O_2 desorption following a very small, but finite dose, i.e. the intercept does not coincide with $(D, \theta) = (0, 0)$.

The sticking coefficient ($s = \mathrm{d}n/\mathrm{d}D = \mathrm{d}(\theta n_s)/\mathrm{d}D$), shown as function of coverage in Fig. 4, has a value of $\sim 0.65 s_{max}$ at very low coverage ($\theta < 0.05$ ML), then increases quickly to s_{max} for $\theta \sim 0.1$ ML. For coverages beyond this value the sticking coefficient decreases in an approximately linear
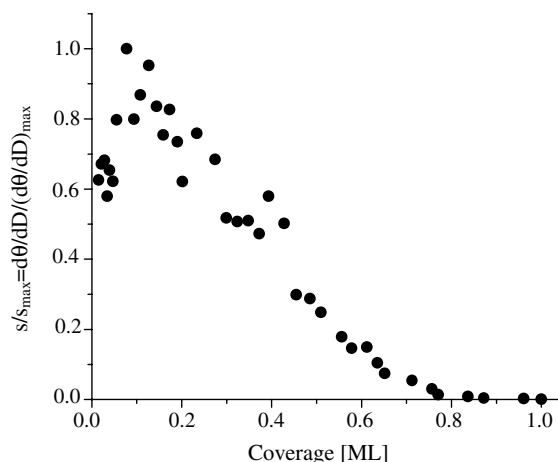

Fig. 4. Normalized sticking coefficient $s/s_{max} = \mathrm{d}\theta/\mathrm{d}D/(\mathrm{d}\theta/\mathrm{d}D)_{max}$ for O/Ir(2 1 0).

---

[1] This statement should be taken somewhat conditionally. Creation of additional adsorption sites might be possible for extremely high doses (e.g. $\sim 10^6$ L).

fashion and reaches a value close to zero for $\theta \sim 0.8$ ML. Maxima in plots of s vs. θ are not common, but have been reported previously [22,23]. The maximum value of the sticking coefficient was found to be $s_{max} = 0.95$, but is contingent on the ionization gauge calibration, hence the use of the relative value s/s_{max}.

The TPD data discussed above were analyzed in detail. The methods described in [24,25] as well as computer simulations were used to determine the desorption parameters. The key results of this analysis can be summarized as follows: oxygen is dissociatively chemisorbed on Ir(210) and desorbs via a second-order process; the desorption process is substantially more complicated than an ideal second-order one, and the activation energy for desorption is variable even for very low coverage. The value for the lowest coverages is $E_d(\theta \to 0) = 4.66$ eV/atom = 449 kJ/mol. The amount of surface oxide formed (by reaction of the chemisorbed oxygen with the substrate) is shown to be insignificant, if at all present. The details of the analysis are presented in Appendix A.

3.2. Structure of the clean and oxygen-covered Ir(210) surface

A typical LEED pattern obtained from the clean fcc Ir(210) surface is shown in Fig. 5a. Based on the specifications of our LEED optics (acceptance angle, working distance) the positions of the diffraction beams (x–y coordinates of the projections on a photographic film or CCD chip) can be calculated for any lattice parameters and incident electron energy (E_e). The result of these kinematic calculations at the same electron energy as the LEED pattern for the Ir(210) surface mesh parameters is shown in Fig. 5b. Comparing Fig. 5a and b shows that the symmetry and size of the reciprocal surface mesh observed by LEED are consistent with the presence of an unreconstructed bulk fcc (210) plane. The LEED beams exhibit strong intensity modulation with change in E_e. This effect is due to the open atomic character of the (210) surface, which allows for strong multiple scattering contributions to the diffracted intensity from all of the exposed layers and is, understandably, absent from the simple kinematic simulation.

When E_e is increased the electron wavelength and, consequently, the diffraction angles decrease, and an apparent motion of the diffraction beams toward the specularly reflected $(0, 0)$ beam is observed (Fig. 5c). For the clean Ir(210) surface the $(0, 0)$ beam is perpendicular to the macroscopic surface plane and is in the center of the LEED pattern. This behavior of the LEED beams is an indication that the surface is both macroscopically and microscopically planar. The result of the kinematic simulation in Fig. 5d supports this conclusion.

No new beams appear in the LEED pattern as a result of oxygen adsorption at 280 K. Notably, an increase in the background intensity (Fig. 5e) is always observed upon oxygen deposition, even for coverages as low as 0.1 ML. The intensity of this background signal increases with exposure and is attributed to additional diffuse scattering from the oxygen overlayer and oxygen induced disorder in the topmost Ir layer.

3.3. Facet formation

The behavior of the oxygen-covered surface upon annealing was found to depend on oxygen coverage. Three different regions of interest (with somewhat blurred boundaries) become evident as the whole range of coverages is explored: low coverage ($\theta < 0.25$ ML), medium coverage (0.25 ML $< \theta < 0.5$ ML) and high coverage ($\theta > 0.5$ ML).

Annealing the crystal when covered with small amounts of oxygen ($\theta < 0.25$ ML) up to 1000 K does not produce new diffraction beams in the (1×1) LEED pattern.

For oxygen coverages $\theta > 0.5$ ML or in the presence of sufficient oxygen background ($p_{O_2} \sim 10^{-8}$–10^{-7} Torr) following a smaller dose, the LEED pattern gradually changes with sample temperature. As the sample temperature is slowly increased (for the purpose of these measurements the rate of temperature increase is low—around 1 K/s or lower) the LEED beams of the initial (1×1) pattern (Fig. 5a) slowly become diffuse and, seemingly, elongate in three different directions or three additional elongated beams appear around them. The transition between a clearly (1×1)
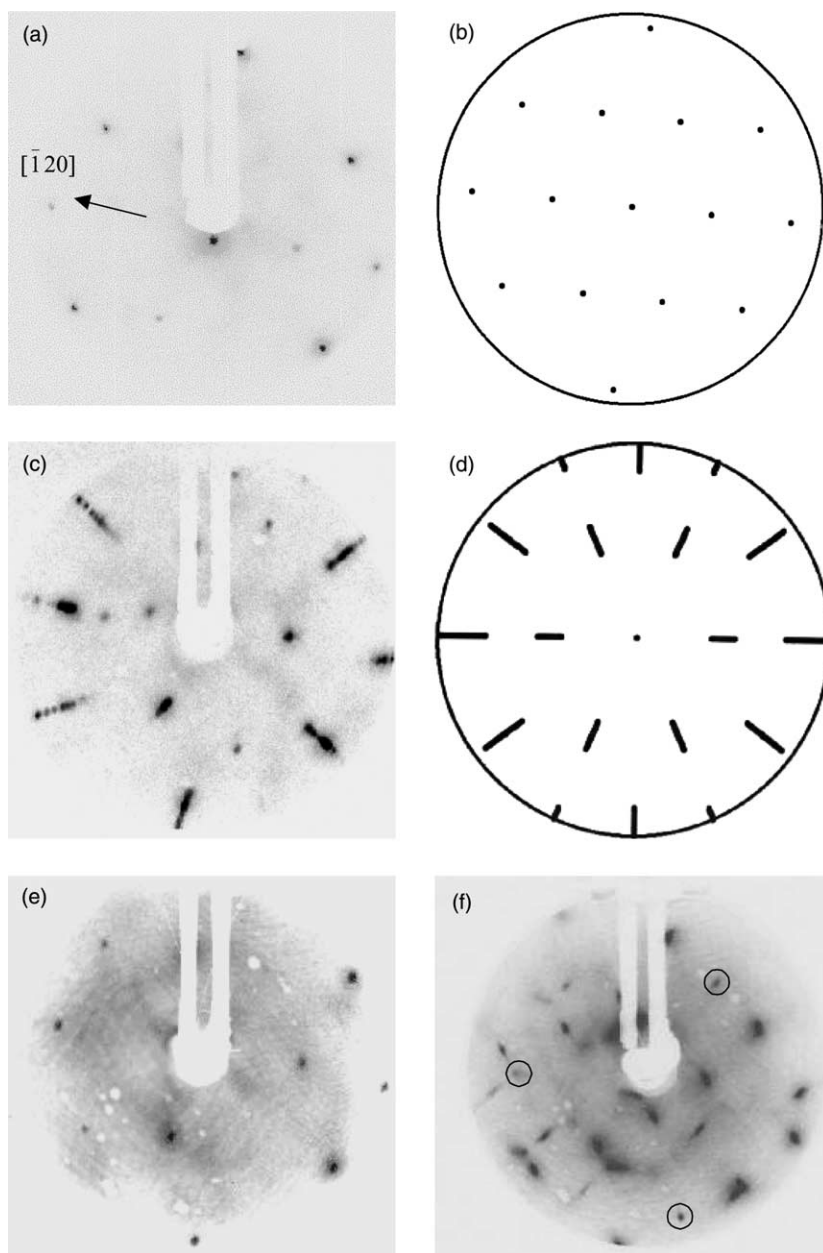
Fig. 5. LEED patterns of Ir(2 1 0) and corresponding kinematic simulations: (a) clean planar, $E_e = 75$ eV; (b) kinematic simulation, same conditions as (a); (c) clean planar surface, $E_e = 50$ to 100 eV; (d) kinematic simulation, same conditions as (c); (e) oxygen-covered planar surface; (f) oxygen-covered surface, after annealing to 600 K. The circles in (f) indicate the positions of three new $(0, 0)$ beams.

pattern and the diffuse one is very gradual and it is difficult to pinpoint accurately the temperature at which it occurs; the lowest temperature at which the pattern is clearly different from the original

(1×1) is approximately 450 K. With further temperature increase the (1×1) beams become progressively fainter, and the emerging new beams become gradually brighter and sharper. This pro-

cess continues until the sample temperature has reached 600 K, when all trace of the (1×1) beams has disappeared, including the specularly reflected $(0,0)$ beam. The emerging beams become clearly separated, and a pattern with a completely different geometry and roughly three times more beams replaces the original one (Fig. 5f).

The temperature evolution of the LEED pattern described above is illustrated in Fig. 6a–d where a part of each pattern has been magnified, and observed as temperature is slowly increased from 300 to 600 K. The sample was pre-exposed to 6 L of oxygen, and the heating performed at $p_{O_2} = 2 \times 10^{-8}$ Torr. The geometry of the LEED pattern does not change with further (above 600 K) temperature increase (up to 850 K, cf. Section 3.5), but changes of the spot size can be observed. This effect can be seen in Fig. 6e–h. It can be observed that the spots are elongated (eccentric) and that this elongation becomes less pronounced as temperature is increased. Subsequent cooling of the sample to room temperature does not reverse the process and the new pattern remains stable and unchanged in the entire temperature range (Fig. 6i).
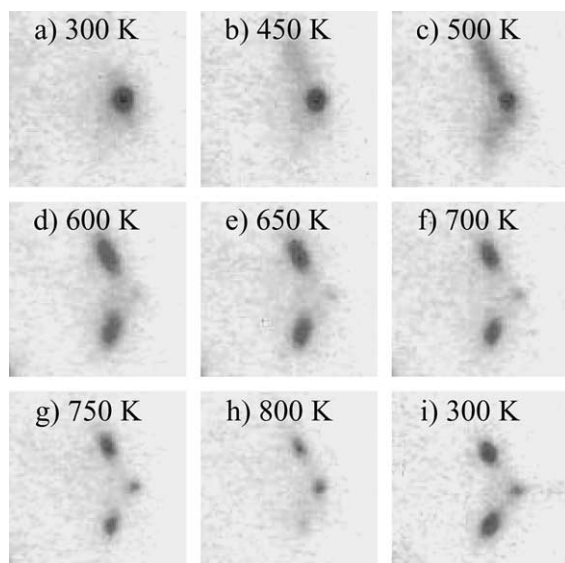

Fig. 6. Evolution of the O/Ir(2 1 0) LEED pattern, $E_e = 90$ eV. The presence of the beams in the LEED pattern and the beam size depend on temperature.

For experiments performed without oxygen in the background gas surface cleanliness is critical: carbon contamination can impede or even completely prevent the occurrence of the described transformations. Initial surface cleanliness is not as crucial when the experiment is performed in oxygen background. The new LEED pattern develops even for a moderately carbon-contaminated surface and remains present provided that the sample is in an oxygen atmosphere or its temperature is comfortably under 600 K.

When E_e is varied the behavior of the new LEED pattern differs from that of the (1×1) (Fig. 7). Rather than converging on the center of the pattern, the diffracted beams move in directions that converge to three distinct points (that is, some beams converge to one point, others to another etc.). Three LEED beams (labeled by small circles in the figure) can be observed, each coinciding with one of the three convergence points. These three beams do not change their positions on the screen when the electron energy is changed, although their intensities vary significantly. They can therefore be identified as specular reflection beams originating from surfaces that are tilted with respect to the $(2 1 0)$ macroscopic surface plane. Moreover, the complete LEED pattern is the superposition of three distinct LEED patterns, whose respective specular directions are each inclined at unique angles (with respect to the macroscopic crystal plane), determined by the crystallographic orientation of the surfaces from which they originate. LEED patterns with similar revealing characteristics have been previously observed in similar experiments, both in this laboratory and others, involving oxygen and metallic overlayers on W(1 1 1) [6,12,13,26–28]. Subsequently, the emergence of these patterns has been interpreted to be a consequence of the formation of nanometer-size facets on the substrate surface.

In addition to requiring a minimum annealing temperature of 600 K, the facet formation process is also dependent on oxygen coverage. In the intermediate range of coverages (0.25 ML $< \theta < 0.5$ ML) changes in the LEED pattern are indeed observed. These changes are similar to those for a fully oxygen-covered surface (close to 1 ML)
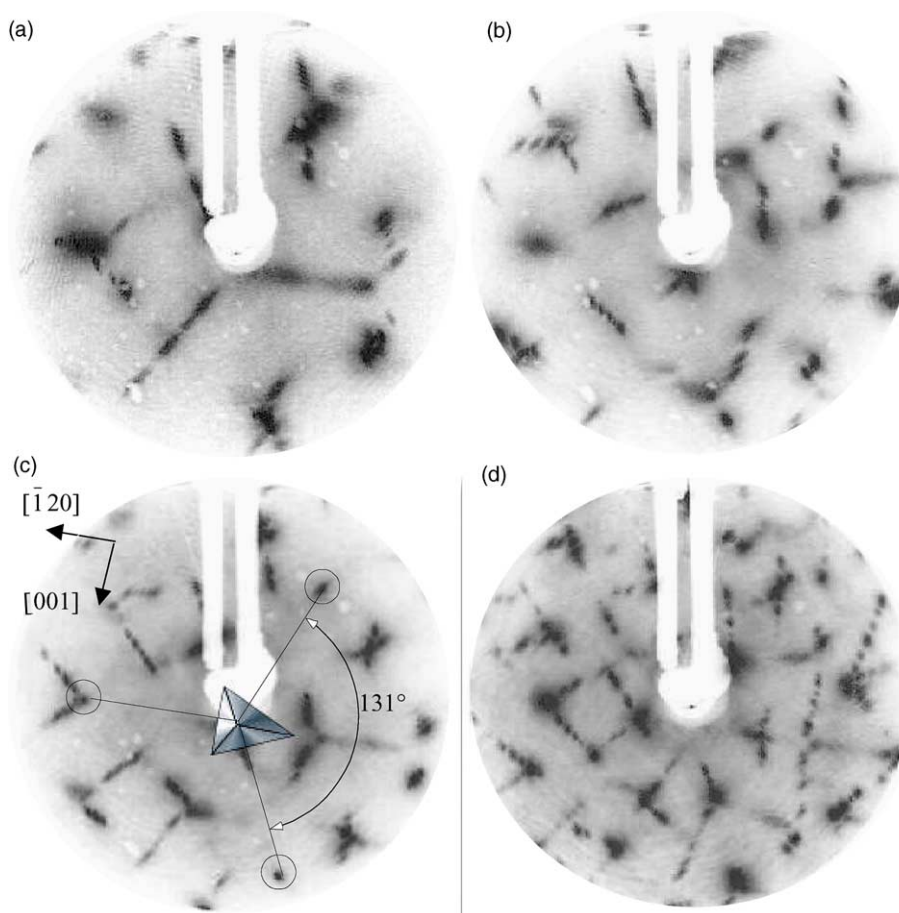
Fig. 7. Variable incident electron energy LEED patterns of the oxygen-covered faceted surface. (a) $E_e = 20$ to 40 eV, (b) $E_e = 45$ to 65 eV, (c) $E_e = 70$ to 90 eV, (d) $E_e = 95$ to 160 eV. The pyramid in (c) illustrates the origin of the specular beams and the azimuthal angle used to determine the facet orientations.

at sample temperatures below 600 K (i.e. blurring of the (1×1) beams, emergence of new beams), but the pattern never evolves into that of the fully faceted surface (e.g. the (1×1) beams do not disappear completely), regardless of the annealing temperature. The lower the coverage in this range, the less apparent the changes are, until they eventually become undetectable by LEED at $\theta \sim 0.25$ ML.

By far the fastest and easiest way to produce a faceted surface is to quickly anneal the sample to a very high temperature ($\sim$2000 K) in the presence of oxygen ($p \sim 10^{-7}$ Torr), and then to cool it in oxygen. In fact, the sample cleaning procedure

(just prior to the final step of high temperature annealing in UHV) invariably results in a faceted surface, even in the presence of moderate amounts of carbon contamination.

Finally, it is noteworthy that the LEED patterns of the faceted surfaces produced by following any of the three procedures described above (slowly annealing an oxygen-covered sample to 600 K in UHV, slowly annealing to 600 K in oxygen atmosphere or flashing to 2000 K in oxygen atmosphere) have geometries identical to those in Figs. 5f and 7 and differ only slightly by LEED spot size.

3.4. Shape and orientation of facets

The LEED patterns of the faceted surface (e.g. Fig. 7) exhibit reflection symmetry with respect to the plane defined by the [2 1 0] and [$\bar{1}$ 2 0] vectors, [2] which is also the plane of reflection symmetry of the bulk crystal. This fact, combined with the presence of three specular spots in the LEED pattern, indicates that the facets are the sides of three-sided pyramids, with reflection symmetry. [3]

To determine the crystallographic orientation of the facets, the position of each individual specular beam is accurately measured. This information is then used to determine the corresponding facet tilt angles (with respect to the (2 1 0) plane), and azimuthal orientation (with respect to each other). For these measurements composite LEED images, constructed by superimposing images of patterns with fixed E_e, were used. Such superimposed images are presented in Fig. 7, where the original LEED patterns were taken at various E_e in the range between 20 and 200 eV. The numerous "dotted lines" in these images are formed by diffraction beams that, due to the changes in E_e between frames, are in a different position on the LEED screen in each individual frame (hence the dotted impression). The specular beams (identified by small circles in the figure) are the only ones that remain at the same positions at all energies. By using the radius of the LEED screen (r_{screen}) and the distance of the specular beams from the center of the pattern (r_{beam}), the corresponding facet tilt angles θ can be calculated (the acceptance angle of the LEED optics is 120°) according to

$$\sin \theta = \frac{r_{\text{beam}}}{2 \times r_{\text{screen}}} \sin 60°. \tag{1}$$

The result for the two symmetric faces of the pyramids is $\theta_1 = 18 \pm 2°$ and for the single face $\theta_2 = 17 \pm 2°$. The angle between the projections of the symmetric facet surface normals on the macroscopic surface plane can be directly measured and is $\phi = 133 \pm 4°$ (see Fig. 7c for illustration). The error bars for all angles are due to the finite size of the specular beams and the uncertainty in determining their positions. Based on these measurements it can be concluded that the two symmetric faces of the pyramids are of (3 1 1) and (3 1 $\bar{1}$) orientations and that the third one is of (1 1 0) orientation. The theoretical tilt angles for these crystal orientations can be calculated from the well-known geometric properties of cubic crystals. The values obtained this way ($\theta_{311} = 19.29°$, $\theta_{110} = 18.44°$ and $\phi_{311} = 131.8°$) and the experimentally obtained ones are in very good agreement. Based on the measured polar and azimuthal angles, no other reasonable choices for the crystallographic orientations of the facets could be found. The array of surfaces considered was very extensive. For the two symmetric faces, all surfaces with indices $(i j k)$, where $-8 < i < 8$, $-8 < j < 8$, $k \in \{1, 2\}$ were considered. Only two of them, besides (3 1 1), have orientations that approximately match the experiment: (7 2 2) and (8 3 2). The corresponding angles are: $\theta_{722} = 18.6°$, $\phi_{722} = 112.3°$ and $\theta_{832} = 14.5°$, $\phi_{832} = 131.8°$. These surfaces were rejected for several reasons. They are atomically rough, high-index surfaces, not likely to lower the surface free energy. The numerical agreement between the calculated angles and the experimentally obtained ones is not as good as in the case of (3 1 1). Finally, they have unit cells considerably larger than those of the (2 1 0) and (3 1 1) surfaces, and create LEED patterns that have many more beams than observed in our experiments. The other possibilities for the single face, (7 6 0) and (8 7 0) were rejected for the same reasons.

Upon close inspection (Fig. 7), it can be observed that the elongation of the LEED spots is face-specific. Recalling that the LEED pattern of the faceted surface is a superposition of three patterns created by the three faces of the pyramids, for each one of these faces, elongation is observed in the same direction for all diffraction spots that belong to the specific face. Due to the small eccentricity, it is difficult to determine the exact direction of the

---

[2] Here only the geometry of the LEED pattern is considered. The spot intensities vary significantly and are not preserved in symmetry transformations.

[3] A LEED pattern with this kind of symmetry could, strictly speaking, also be produced by a conveniently distributed assortment of domains of various sawtooth-like structures. However, previous experiments involving facet formation have not revealed any such structures. More importantly, our preliminary STM experiments support the three-sided pyramid interpretation.

elongation. In the case of the (1 1 0) face, this direction closely coincides with the direction along the atomic rows of the (1 1 0) surface. For the {3 1 1} faces the elongation seems to be slightly offset from the direction along the atomic rows on the {3 1 1} faces, but the angle between them is small (~4°) and is comparable to the error in measurement. The direction of atomic rows was calculated for ideal (1 1 0) and {3 1 1} surfaces.

3.5. Reversible facet destruction (relaxation) and reconstitution

The oxygen-covered faceted surface exhibits interesting behavior at temperatures above the 600

K that is necessary to cause facet formation. As temperature is increased from 600 to 850 K, no effect on the geometry of the LEED pattern is observed. Although the beam intensities gradually decrease with temperature increase, at fixed energies E_e the positions of individual spots remain invariant at all temperatures in this interval. Furthermore, the LEED beams continue to converge toward the off-center specular beams when E_e is increased (Fig. 8), indicating that the surface remains faceted. However, when the sample temperature reaches approximately 850 K, the beams corresponding to the faceted surface completely disappear and beams corresponding to the original planar surface reappear in the LEED pattern. Upon cooling, the re-
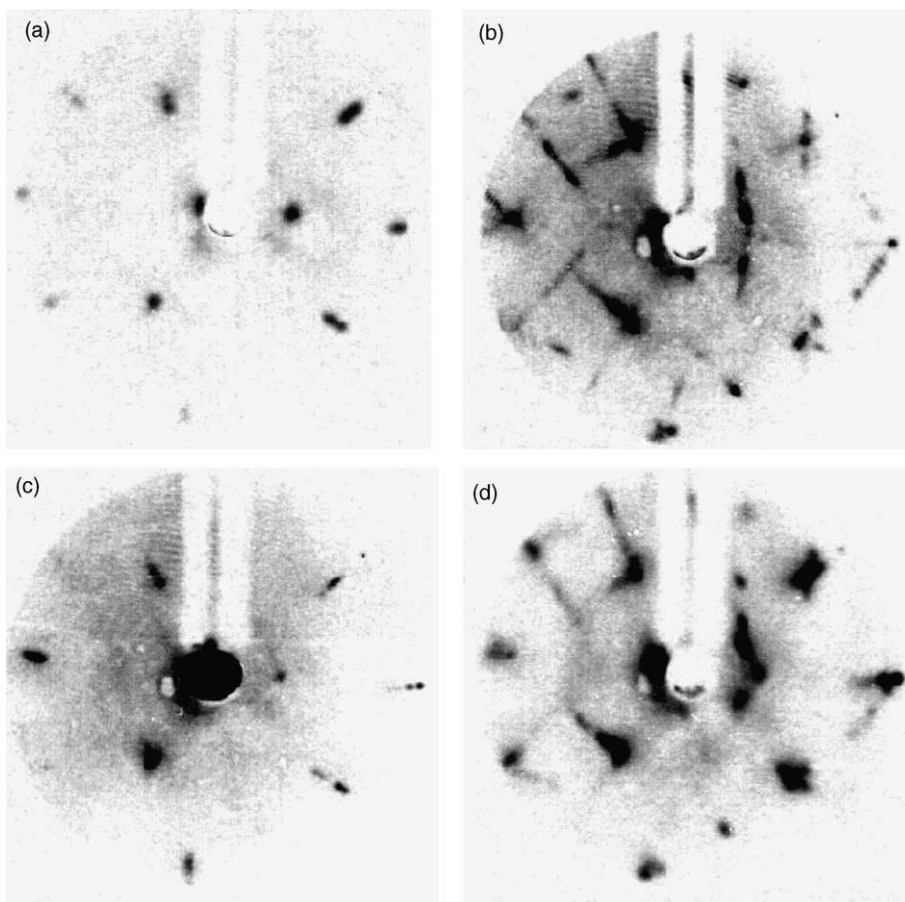

Fig. 8. Variable energy ($E_e = 50$ to 100 eV) LEED patterns of oxygen-covered Ir(2 1 0) surface during a temperature cycle: (a) planar, $T = 290$ K; (b) faceted, $T = 650$ K; (c) planar, $T = 890$ K; (d) faceted, $T = 290$ K. The sample itself is clearly visible in (c) because of its glow.

versed process is observed: the beams corresponding to the planar surface disappear, and the beams corresponding to the faceted surface reappear. The sample temperature can be cycled repeatedly to alternate between the faceted and planar surface structure. Using the current experimental setup, it was not possible to determine whether the transformation occurs at the same temperature in both directions. It is important to note that, if performed in UHV with an oxygen-covered sample, this procedure is critically dependent on the cleanliness of the surface, mainly of carbon contamination: if the sample is very clean the patterns deteriorate only gradually and become ill-defined during the course of several heat–cool cycles.

In cases of higher carbon concentration, the faceted pattern promptly and irreversibly disappears (the surface *relaxes* into its original planar state) upon heating at temperatures as low as 600 K. Under conditions of such carbon contamination facets can be only formed by heating the sample in oxygen atmosphere, not by heating an oxygen-covered sample in UHV. Traces of carbon (see Section 2) remain present as contamination even after the most thorough of our cleaning procedures and cause gradual oxygen loss (due to reaction with carbon impurity on the surface and with H_2 and CO adsorbed from the residual gas). We suspect that this is the cause for pattern deterioration during various LEED measurements at elevated temperatures in UHV and, ultimately, relaxation of the facets at 600 K.

3.6. The clean faceted surface—"Freezing" the facets

An aspect entirely new to overlayer-induced faceting experiments is the production of a clean faceted iridium surface. This has been, for various system-specific reasons (e.g. overlayer and substrate properties), either not possible or not demonstrated in previous studies of this kind. The most straightforward method of removing oxygen from the iridium surface is through thermal desorption, as used in the sample cleaning procedure. However, this method is useless if the objective is to produce a clean faceted iridium surface, because the faceted surface reverts to planar at 600 K (in the absence of oxygen) and at 850 K (when oxygen is present on the surface). These temperatures are significantly lower than those required to completely remove the oxygen by desorption ($\sim$1400 K) making it impossible to remove the oxygen by desorption without destroying the faceted surface. However, our investigations have revealed two "low temperature" procedures for circumventing this problem, by chemically removing the oxygen overlayer.

The first such method takes advantage of catalytic CO oxidation in the following manner: commencing with a faceted surface (Fig. 9a)
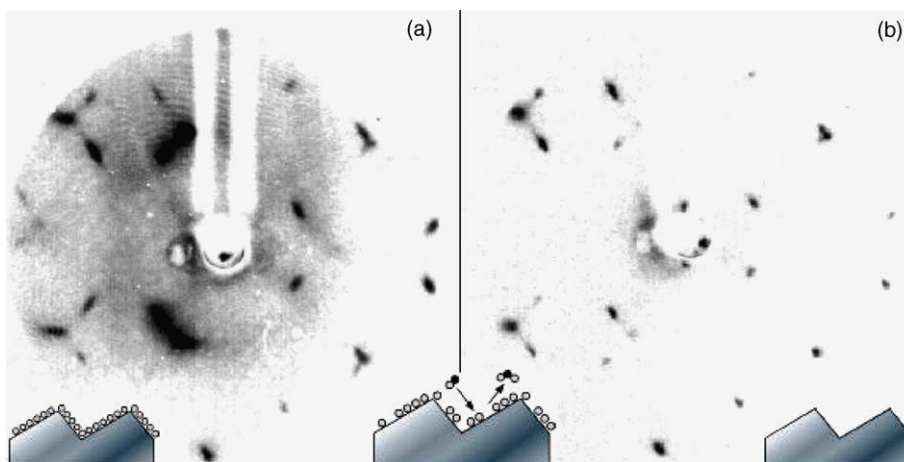

Fig. 9. LEED patterns ($E_e = 75$ eV) of the oxygen-covered faceted surface (a) and of the clean faceted surface (b). On the bottom left and right are schematic drawings of these surfaces. The drawing in the middle illustrates the cleaning reaction.

completely covered with oxygen, the temperature of the sample is set to 500 K and then CO is leaked into the chamber at a pressure of 5×10^{-9} Torr. As expected (Eq. (2)), a surface reaction occurs,

$$CO_{(ad)} + O_{(ad)} \rightarrow CO_{2(g)} \qquad (2)$$
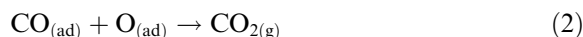
which results in an increase of the CO_2 signal (typically by a factor of $\sim$4) in the residual gas mass spectrum. When the integrated CO dose has reached 1.2 L (after $\sim$240 s) the CO is pumped from the chamber and the sample temperature is increased further (to $\sim$550 K) and held at that temperature (in UHV) for additional 2 min, in order to desorb any excess CO. Upon cooling to room temperature the surface retains its faceted structure, as verified by LEED (Fig. 9b). TPD measurements following this procedure reveal that only trace amounts of CO and O_2 desorb, confirming that an atomically clean faceted surface has been produced (Fig. 10). [4] The amount of CO remaining on the surface decreases if the annealing temperature in the second part of the cleaning procedure is increased. When the temperature reaches $\sim$580 K, CO becomes undetectable on the surface [29]. When annealed, the clean faceted surface, as expected, irreversibly reverts to planar at 600 K.

While the catalytic CO oxidation procedure is successful for producing a clean faceted Ir surface, the use of a carbon-containing molecule is a slight drawback and it is good practice not to use more CO than is necessary. Temperature control is also a sensitive issue, since the sample temperature in the second part of the process approaches 600 K and inaccuracies can lead to facet relaxation.

In order to improve on these two limitations, a similar procedure was adopted, replacing CO with hydrogen to remove surface oxygen, according to the reaction:

$$H_{2(g)} + O_{(ad)} \rightarrow H_2O_{(g)} \qquad (3)$$

In this case the sample temperature is set to only 400 K; H_2 is then temporarily introduced into the
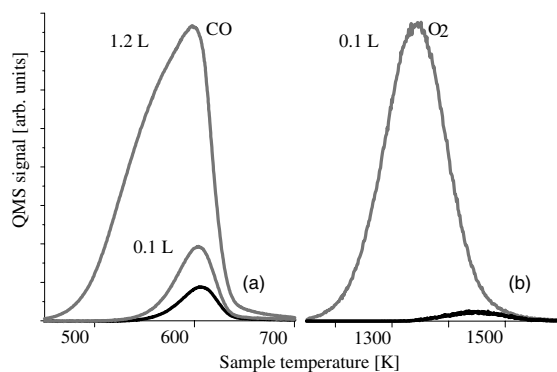

Fig. 10. TPD spectra of CO (a) and of oxygen (b) left over (black lines) after the cleaning procedure described in Section 3.6. The 1.2 L exposure of CO was chosen for comparison in order to match the CO dose that was used in the cleaning procedure.
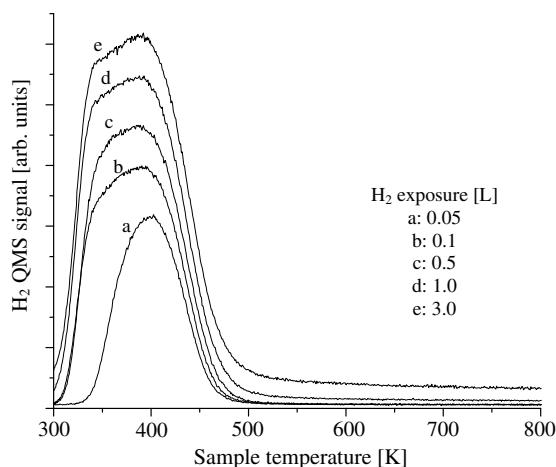

Fig. 11. TPD spectra of H_2/Ir(2 1 0) deposited at room temperature.

chamber (usually backfilled to a pressure of 5×10^{-9} Torr for 200 s, resulting in a 1 L exposure). The H_2 is subsequently pumped out, and the sample kept at 400 K in UHV for additional 120 s before cooling to room temperature. This temperature is sufficient to ensure the desorption of both hydrogen (Fig. 11) and water [29–31]. This procedure results in a clean faceted surface, with the added benefit that the sample temperature remains comfortably lower than 600 K at all times. In both cases (i.e. for surface oxygen removal by CO and H_2) the surface remains "frozen" in its faceted state at temperatures up to 600 K.

---

[4] By comparing Fig. 9a and b a decrease in background intensity can be observed. This is also an indication, albeit a very crude one, of adsorbate removal.

The clean faceted surfaces produced using these two procedures appear identical in LEED and AES. Similarly, the respective surface reactivities (as observed in acetylene decomposition experiments) are identical [29].

3.7. High resolution soft X-ray photoelectron spectroscopy and surface chemistry

The results of our detailed investigations of the photoemission and surface chemistry experiments are reported elsewhere [31,32], and here we only summarize the main conclusions. Photoemission experiments carried out in this research effort were focused on studying the shallow 4f core level electronic states of iridium. The 4f electronic states of individual iridium atoms are particularly sensitive to the presence of the surface termination or adsorbates and exhibit chemical shifts in their binding energy (up to ~1 eV, depending upon the local chemical environment). The differences between the 4f photoemission spectra of the faceted and planar surfaces were found to be minimal, but the spectra were significantly influenced by the presence of oxygen overlayers on these surfaces.

Surface chemistry experiments show that the Ir(2 1 0) surface is very active for the thermal catalytic decomposition of acetylene to hydrogen [31]. Marked differences were observed in reaction rates on the planar and faceted surfaces. This is an indication that the morphology of the surface plays a considerable role in the kinetics of the reactions involved, a sign of their structure sensitivity.

4. Discussion

4.1. Oxygen adsorption and desorption

The sticking coefficient for room temperature O/Ir(2 1 0) adsorption (Section 3.1, Fig. 4) shows interesting behavior: after increasing by a factor of ~1.5 in the 0 ML $< \theta <$ 0.1 ML region, it steadily decreases for coverage $\theta >$ 0.1 ML. In the latter case the dependence on coverage closely resembles the predictions of the Kisliuk model for $K = 0$ [33]. In this model, the probability of chemisorption is

considered in terms of adsorption and desorption probabilities for a physisorbed precursor molecule on the surface. P_a is the probability of chemisorption for a precursor molecule physisorbed over an unoccupied site, P_b is the probability of desorption if the site is unoccupied, and P'_b is the probability of desorption if the site is occupied. K is a function of these elementary probabilities: $K = (P'_b - P_a)/(P_a + P_b)$. Although not usually observed, an increase of the sticking coefficient in the low coverage region is not unprecedented: such behavior occurs in some systems in the course of molecular chemisorption (e.g. N_2/Ru(0 0 1) [22]) and dissociative chemisorption (e.g. O/W(1 1 0) [23]). This behavior may indicate an adsorption and nucleation process that is facilitated by the presence of the adsorbate gas on the surface (e.g. adsorption could be facilitated on the edges of islands of adsorbed oxygen). There are several possible sources of error in the estimation of oxygen coverage (e.g. ion gauge calibration and oxygen loss due to chemical reactions, discussed later in this section); however, these have little or no influence on error in the determination of the sticking probability because the desorption signal is differentiated and normalized, and they cannot account for the observed maximum in s vs. θ.

The structural changes (throughout the faceting transitions, cf. Fig. 6) discussed earlier have a strong bearing on the analysis and interpretation of the TPD spectra. Desorption is usually presumed to occur from an adsorbate layer on a more or less rigid substrate, but for desorption in the O/Ir(2 1 0) system this is clearly not the case. As LEED experiments show, when enough oxygen is present, the surface undergoes two major structural transformations (Sections 3.3 and 3.5, Fig. 8) in the temperature range covered by a TPD measurement: Facet formation occurs at 600 K and facet relaxation takes place at 850–900 K. A TPD measurement typically starts by heating from 300 to 500 K without data acquisition, a time during which transient deviations from linearity of the heating rate die away. Acquisition begins at 500 K and finishes at 1650 K (Fig. 2), but heating continues at a linear rate up to 1750 K in order to provide a reliable set of data points for background corrections. The range of temperatures

over which desorption occurs varies with oxygen coverage and spans between 650 and 1450 K.
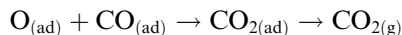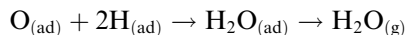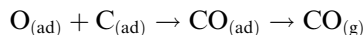
Structural changes begin to occur for coverages in the $\theta < 0.5$ ML region, and their magnitude and influence on the TPD measurements increase with coverage increase. For coverages close to 0.5 ML facets are formed at temperatures for which little desorption occurs (~ 600 K), but facet destruction coincides with moderate to high desorption rates (~ 900 K). For coverages close to 1 ML both facet formation and facet destruction occur during a TPD measurement. The latter certainly has a major influence on the measurements because of the high (close to peak) desorption rate at 750–850 K. Under the above conditions, desorption occurs from the three distinct and identified surfaces: the planar (2 1 0) and the two non-equivalent faces of the pyramids (namely the {3 1 1} and (1 1 0)), and possibly from any number of transition surfaces that have not been identified [5] (surface roughening prior to facet formation has been reported for the Pt/W(1 1 1) system [34]). Furthermore, the possible existence of more than one state of chemisorbed oxygen cannot be a priori excluded for any of these surfaces. Two peaks associated with chemisorbed oxygen have been observed using TPD in O/Ir(1 1 0) adsorption experiments [35].[6] This creates a situation in which the surface structure depends on oxygen coverage (and temperature), and (through the desorption rate) the oxygen coverage depends on the surface structure. Two major complications are therefore present in interpreting TPD spectra of O/Ir(2 1 0): (a) the surface structure is characterized by several crystal orientations; (b) the surface structure and desorption rate are mutually dependent. In order to minimize the effect of these complications, in the analysis and interpretation of TPD spectra described in Appendix A only exposures lower than 0.5 L ($\theta = 0.32$ ML) have been considered. This provides enough margin to ensure that the effects

of the observed oxygen-induced surface structural transformations are of as little consequence as possible.

The results of the analysis in Appendix A clearly show that the desorption kinetics are complex and not consistent with a simple second-order desorption process, even for coverages as low as 0.1 ML. This behavior may be a consequence of complicated adsorbate–substrate interactions. Indeed, although facets fully cover the surface for 600 K $< T <$ 850 K and 0.5 ML $< \theta <$ 1 ML, and partial faceting occurs already at 450 K and 0.25 ML, structural changes likely occur for lower coverage and temperature. The main indication for the existence of such changes is the increase in the background intensity of the LEED patterns upon oxygen deposition (cf. Section 3.2). Interpreted as a consequence of scattering from the oxygen overlayer and, more importantly, oxygen induced disorder of the Ir(2 1 0) surface, the effect can be observed for coverages as low as 0.1 ML and is present even at room temperature. Under such conditions, the assumption of a desorption process occurring from sites situated on a relatively rigid substrate could be invalid.

Formation of surface oxides on Ir(1 1 1) and Ir(1 1 0) has been observed in previous experiments [35,36] upon thermal activation (between 700 and 1200 K in oxygen atmosphere). In the experiments discussed in this paper, oxygen deposition for the purpose of obtaining TPD spectra was always performed at room temperature and oxides, if at all formed, were found to amount to an equivalent of less than 10^{-3} ML of oxygen.

Another minor point that was considered is the x-intercept observed in the uptake curve in Fig. 3. This is an effect that can be caused by processes on the iridium surface, as well as by experimental errors. Oxygen loss from the adsorbed layer after deposition can occur due to a variety of chemical reactions:

$$O_{(ad)} + C_{(ad)} \rightarrow CO_{(ad)} \rightarrow CO_{(g)}$$
$$O_{(ad)} + 2H_{(ad)} \rightarrow H_2O_{(ad)} \rightarrow H_2O_{(g)}$$
$$2O_{(ad)} + C \rightarrow CO_{2(ad)} \rightarrow CO_{2(g)}$$
$$O_{(ad)} + CO_{(ad)} \rightarrow CO_{2(ad)} \rightarrow CO_{2(g)}$$

---

[5] Because of the high heating rate the faceting transition may not be complete before the onset of desorption (~ 650 K).

[6] Since no faceting has been observed for the O/Ir(1 1 0) system, we must conclude that both chemisorbed states belong to the (1 1 0) face itself.

Systematic errors in measuring the O_2 exposure (in this case an underestimate of the integrated area under the pressure vs. time curve) can also contribute to the observed effect. In both cases the error caused in determining the coverage vs. exposure dependence would be constant or depend weakly on exposure.

4.2. Facet formation and destruction; thermodynamics vs. kinetics

4.2.1. Oxygen-covered surface—facet formation

The presence of planar 1×1 and faceted surface beams for temperatures between 450 and 600 K (Fig. 6) indicates the coexistence of planar and faceted surface regions. As the temperature is increased, the surface becomes partially faceted, with facet size smaller than the coherence length of the electron beam (hence the diffuse LEED spots). The relative intensities of the planar 1×1 beams and the faceted beams reflect the ratio of surface areas of the coexisting planar and faceted regions of the surface. The absence of 1×1 beams between 600 and 800 K shows that the surface is completely faceted. The observed decrease of faceted spot size in this temperature region (and in the coexistence region between 450 and 600 K) is an indication of facet growth. A similar effect has been observed in facet formation of platinum covered W(1 1 1) [37].

In a macroscopic description, the mathematical treatment of facet formation on the surface of a solid is often based on considerations involving the equilibrium crystal shape (ECS) of a small crystal. The ECS is determined by the surface free energy γ_i, expressed in units of energy per unit area, where **i** is a crystallographic orientation. In the absence of external forces the ECS of a small crystal (with constant volume) has the minimum total surface free energy $E = \sum \gamma_i A_i$ (A_i is the surface area of the crystal with crystallographic orientation **i**), and can be determined by using Wulff's construction [38]. The anisotropy in surface free energy ($\Delta\gamma = \gamma_i - \gamma_j$, where $\gamma_i \neq \gamma_j$ for two crystallographic directions **i** and **j**) that determines the ECS of a small crystal can cause facet formation on the planar surface of a macroscopic crystal. When this occurs, the original planar surface is (partially or completely) replaced by a surface (or assortment

of surfaces) with larger total surface area, but smaller total surface free energy. The facets typically have linear dimensions only in the range of tens to hundreds of Angstroms, and a faceted crystal invariably remains macroscopically planar. Facets usually expose surfaces that are close packed, corresponding to low index crystal planes, such as bcc (1 1 0) and fcc (1 1 1). These surfaces have lower γ_i compared with more atomically rough surfaces like bcc (1 1 1) and fcc (2 1 0), which have been found to exhibit overlayer-induced faceting [3,12].

For fcc Ir both the {3 1 1} and (1 1 0) surfaces are more closely packed than (2 1 0) (ideal fcc {3 1 1} and fcc {1 1 0} surfaces are illustrated in Fig. 12). The density of atoms in the top surface layer for the ideal {3 1 1} and (1 1 0) surfaces is larger than for the (2 1 0) surface: $n_{(210)} = 6.04 \times 10^{18}$ m^{-2}, whereas $n_{(311)} = 8.15 \times 10^{18}$ m^{-2}, $n_{(110)} = 9.56 \times 10^{18}$ m^{-2} (for the most close-packed surface of Ir, $n_{(111)} = 1.56 \times 10^{19}$ m^{-2}). The exposed surface area of a pyramid (sides only, excluding the base) formed by these planes on Ir(2 1 0) is 5.8% larger than the area of the planar surface on which it forms.

The necessary condition for facet formation as derived from surface free energy considerations can be expressed as follows:

$$S_1\gamma_{(311)}/\cos(\theta_{311}) + S_2\gamma_{(110)}/\cos(\theta_{110}) - \gamma_{(210)} < 0, \quad (4)$$

where $\theta_{311} = 19.29°$ and $\theta_{110} = 18.44°$ are the facet tilt angles and $S_1 = 0.7$ and $S_2 = 0.3$ are normalization coefficients that take into account the partial contribution of each of the {3 1 1} and (1 1 0) surfaces to the total surface area of one pyramid. Essentially, Eq. (4) states that faceting can occur only if the increase in surface area (reflected by the cosines in the denominators) is compensated for by an appropriate difference in surface energy anisotropy (to $\Delta\gamma/\gamma > 5.8\%$ in the case of O/Ir(2 1 0)). For clean metal surfaces the anisotropy in surface free energy is generally too small for an atomically rough surface to spontaneously form a faceted structure. Field-ion microscopy (FIM) and field-electron microscopy (FEM) measurements, although not performed on
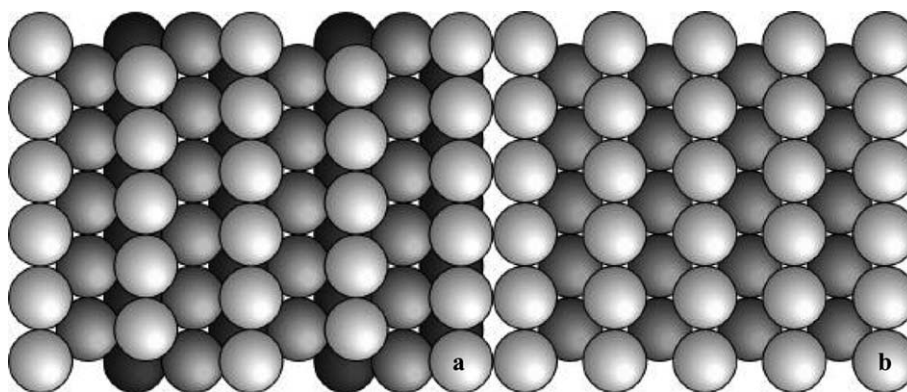
Fig. 12. Hard sphere models of the fcc (3 1 1) (a) and fcc (1 1 0) (b) surfaces.

crystals of fixed volume (due to constant blunting of the tip by self-diffusion [39]) can provide a rough estimate of the surface free energy anisotropies. For clean iridium FIM measurements at $T = 1360$ K indicate $\Delta\gamma_{(210)}/\gamma_{(110)} \sim 0.3\%$ and $\Delta\gamma_{(210)}/\gamma_{(311)} \sim 1\%$ only [40]. Clearly, such a small anisotropy (even when reasonably extrapolated to higher values at lower temperatures) is not sufficient to satisfy (Eq. (4)) and drive a transformation that results in a 5.8% increase in surface area. Adsorbed layers on the surface, however, can significantly change this situation.

The presence of adsorbates can reduce the surface free energy of some crystal planes, which results in an increase in $\Delta\gamma/\gamma$ [10]. This can, in turn, satisfy (Eq. (4)) and make a faceted surface thermodynamically more stable and favorable compared to a planar one. In view of this, it is plausible that some minimum oxygen coverage is necessary to cause a change in γ (and $\Delta\gamma/\gamma$) large enough to make facet formation possible. In W(1 1 1) faceting experiments involving metallic overlayers, a minimum coverage of one physical monolayer was found to be necessary for facet formation [34].

Additionally, a further thermodynamic driving force may arise from edge energy minimization. The total surface free energy that includes the contribution from edge energy can be expressed as $E = \sum \gamma_\mathbf{i} A_\mathbf{i} + \sum \Gamma_\mathbf{j} l_\mathbf{j}$ ($\Gamma_\mathbf{j}$ is the edge free energy per unit length along the $\mathbf{j}$ crystallographic direction). Although without influence on facet orientation, the edge energy component can affect the equilib-

rium pyramid size [12,41] (a surface covered with larger pyramids has a smaller total edge length).

Even though facet formation can be thermodynamically favored, there may be kinetic limitations to facet formation: that is, the faceted surface does not replace the planar one until a minimum sample temperature has been reached. [7] This can be interpreted in a relatively straightforward way: the surface diffusion rate of iridium atoms at and below room temperature is too low for any significant mass transport to occur. Although 1D and 2D self-diffusion of iridium has been observed in field emission experiments at and below room temperature [42,43], it is only at elevated temperatures ($\sim$530 K) that diffusion over step edges was found to be sufficient to cause changes in the size of the planar regions of emitter tips [44]. Considering the typical size of each pyramid, reflected most importantly in the number of atoms in each (for the usual linear dimensions in the range of tens to hundreds of Angstroms this is $\sim 10^2$–10^4 atoms) and the distances over which they need to be transported in order to form it, it is understandable how a low surface diffusion rate can render the process of facet formation unobservably slow, if it occurs at all. It can therefore be said that the deposition of oxygen on the Ir(2 1 0) sur-

---

[7] On the time scale of our experiments: we observed no signs of facet formation at room temperature on a sample that has been fully oxygen-covered for $\sim$15 h.

face at room temperature effectively leaves it "frozen" in a non-equilibrium state.

Further conclusions can be drawn from the fact that, even though complete faceting is not achieved for temperatures $T < 600$ K $= 0.22T_m$, LEED shows background increase at room temperature, obvious and gradual changes in structure that commence at $T \sim 450$ K $\sim 0.17T_m$ and become more apparent with temperature increase. As in other diffusion processes, many potential barriers of varying height can exist along the path of an atom that is being incorporated in a pyramid [45]. Depending on the height of potential barriers throughout the process, a minimum temperature may exist, above which kinetic barriers can be overcome in reasonable time and enable the surface to reach a particular low-energy state. Considering the extent of the surface transformation, the diffusion process during facet formation is undoubtedly complicated by the fact that these paths lie on a potential surface that changes along with the changes of the surface structure.

In view of the above discussion it can be concluded that facet formation is a thermodynamically driven and a kinetically limited process, just as in many other overlayer-induced faceting experiments (e.g. [6,13]).

4.2.2. Oxygen-covered surface—facet destruction

The oxygen-covered faceted surface transforms to a planar surface at a sample temperature of $T \sim 850$ K (Section 3.5). In this process the roles of kinetic limitations and thermodynamic driving force are not the same as during facet formation at 600 K. Since the clean faceted surface reverts to planar at 600 K (Section 3.6), it is evident that at that temperature (and any higher one) there is enough thermal energy to overcome any kinetic limitations involved in the process, and one has to conclude that facet destruction is driven by a change in free energy that occurs due to a temperature dependence of $\gamma_i = \gamma_i(T)$. Indeed, surface free energy anisotropy generally decreases with increasing temperature and becomes zero at the melting point T_m [46]. The situation is illustrated in Fig. 13, where the total free surface energy $E(T) = \sum \gamma_i(T) * A_i$ of the planar and faceted surfaces is schematically plotted. Over the entire
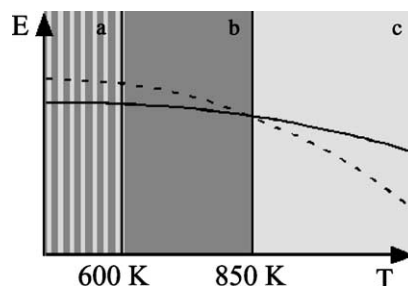

Fig. 13. Schematic plot of the free energy of the oxygen-covered planar (dashed line) and of the faceted surface (solid line). The state of the surface (planar/faceted) is different in the three distinct temperature regions. In (a) the surface state depends on its history; in (b) it is always faceted; in (c) it is always planar.

temperature interval the ratio of the planar and faceted surface areas (a purely geometrical quantity) is a constant $A_{fac} = 1.058 * A_{210}$, independent of temperature. Therefore, the value of $\Delta E = E_{fac} - E_{210}$ is influenced only by the temperature dependence of γ. For $T < 850$ K, $\Delta E < 0$, the facet formation condition in Eq. (4) is satisfied and facets are immediately formed once enough thermal energy is available to overcome kinetic limitations. As the temperature increases, surface free energy anisotropy decreases $(\gamma_{(311)}(T) - \gamma_{(210)}(T) \to 0$ and $\gamma_{(110)}(T) - \gamma_{(210)}(T) \to 0)$ and at ~ 850 K a crossover occurs and the situation reverses (from $\Delta E < 0$ to $\Delta E > 0$). When this takes place, the condition in Eq. (4) is no longer satisfied and the surface subsequently "defacets" (see Fig. 8) regardless of ample oxygen presence. [8] A very similar phenomenon has been observed for O/Mo(1 1 1) [6].

4.3. The clean faceted surface

The phenomenon of "freezing" (as detailed in Section 3.6) an otherwise unstable surface by temporarily stabilizing it with an adsorbate and then chemically removing the adsorbate at reduced

---

[8] The values of $\Delta\gamma_{(210)}/\gamma_{(110)}$ and $\Delta\gamma_{(210)}/\gamma_{(311)}$ could, in principle, at some low temperature, exceed the values necessary to make the faceted surface stable, even in the absence of an adsorbate. We have no way of experimentally verifying if this indeed happens.

temperature has been observed for reconstructions of Pt(1 0 0) [47] and Ir(1 0 0) [48]. In the case of Ir(2 1 0) the motivation for attempting to accomplish this on a larger scale and produce a clean faceted surface is twofold:

(a) The microscopic processes involved in facet formation are not well understood. A clean faceted surface is the most simple system on which one can experimentally probe and subsequently theoretically model the facet relaxation process (i.e the faceted → planar transformation). It is, for example, clear that significant substrate mass transport must occur in order to create such large (on atomic scale) structures that are completely absent from the planar surface. Whether this transport involves diffusion from and into the crystal bulk, surface diffusion, diffusion along various step edges or a combination of the above, is presently unknown. Furthermore, the modes of mass transport for facet creation and relaxation are not necessarily identical.

The role of each mode of mass transport involved in the faceting transition will vary depending upon the facet size, and measuring characteristic relaxation times as function of pyramid dimensions can help deduce the role of each of them play. Although such measurements can, in principle, also be performed on an oxygen-covered surface at ∼850 K, the clean surface is a simple, single-component system and any contribution toward morphological transformations by the presence of an adsorbate are eliminated. Likewise, the use of the clean, faceted surface ensures that process modeling and first principle calculations can be performed with relative ease. Additionally, the faceting ↔ planar structural transitions on Ir(2 1 0) occur at temperatures that are quite accessible to existing variable-temperature scanning probe techniques.

(b) Faceted Ir(2 1 0) provides an excellent substrate for studying the sensitivity of chemical reactions to the surface morphology (or structure) of the catalyst. Structure sensitivity of chemical reactions has been studied in detail in metal/W(1 1 1) faceting related experiments [17,18]. In those experiments, structure sensitivity is found to be exhibited in butane hydrogenolysis, reactions of chemisorbed benzene, as well as for reactively-

formed (from adsorbed acetylene) ethylene and benzene. Monte Carlo simulations suggest that the desorption kinetics on nanoparticles that expose two different crystal faces can be dramatically different from that expected by a simple superposition of the kinetics on infinitely large individual crystal faces [49]. An additional benefit that the absence of an adsorbate on the faceted surface can bring is that it simplifies the situation (e.g. from the surface electronics properties point of view) because only the substrate material is present. There are also no agglomerates of unordered excess overlayer material that can give contributions to the results.

It was detailed earlier (Section 3.3) that the surface transition from planar to the faceted structure for oxygen-covered iridium (2 1 0) has its onset at $T \sim 450$ K. It has also been established that the iridium surface, in the absence of the oxygen overlayer, remains planar at all temperatures. Therefore, if the surface, upon removal of the oxygen overlayer, were to revert from the faceted structure to the planar (2 1 0) at a temperature close to that observed for faceting onset, the removal of the oxygen overlayer would necessarily have to be achieved at temperatures below 450 K in order to preserve the facets. Indeed, this obstacle seemed insurmountable and the ability to produce a clean, faceted surface was initially thought impossible. Experimental evidence shows (as described in Section 3.6) that the surface can be cleaned to remove oxygen by reaction with CO at a temperature of 550 K, while maintaining its faceted structure. This disparity in the onset temperatures for the two processes (∼450 K for facet formation and 600 K for destruction) indicates that the kinetic barrier for facet formation (on the oxygen-covered planar surface) is higher than the barrier for facet destruction (on the clean faceted surface). An explanation of this phenomenon can be offered in terms of the differences between the two surfaces on which the processes occur: in one case an oxygen layer is present on the surface, in the other it is not. Adsorbed oxygen has been found to increase the surface mobility of iridium atoms on emitter tips and decrease the annealing temperature necessary to cause tip facet rearrangement by

	CLEAN		OXYGEN-COVERED
PLANAR	STABLE	**oxygen deposition** →	METASTABLE
	annealing ↑		↓ **annealing**
FACETED	METASTABLE	← **removal of adsorbed O by CO or H₂**	STABLE

Fig. 14. States and transformations of the Ir(2 1 0) surface.

about 200 K [44], an effect with sufficient magnitude to account for the facet stability on Ir(2 1 0). STM experiments with H/Pt(1 1 0) reveal similar adsorbate-induced enhancement of surface self-diffusion [50].

The table in Fig. 14 illustratively summarizes the morphological transformations and states of the substrate/adsorbate system occurring throughout a cycle of oxygen deposition, facet creation, oxygen removal and facet destruction:

The deposition of oxygen on the planar Ir(2 1 0) at room temperature changes the surface energy in a way that makes the faceted surface a thermodynamically favorable (i.e. a stable) state. The pre-existing, initially stable, planar surface is altered to one that is metastable, in which the system remains "frozen" because the deposition temperature is low ($\sim$300 K). Although it is energetically favorable for facets to form, this does not occur because the mobility of substrate atoms is insufficient. In this situation, only through annealing the surface can the transition to produce the more stable, faceted state occur.

When oxygen is chemically removed from the faceted surface at low temperature, the reverse situation to the one just described occurs. In this case it is the planar (2 1 0) morphology and not the clean faceted structure, that has the lower surface energy. The faceted state, in turn, becomes one that is metastable and owing to the low sample temperature, the surface does not revert to its planar structure due to insufficient mobility of the iridium atoms. Instead, it remains "frozen" in its faceted state. Again, the transition (this time into the more stable, planar state) only occurs at elevated sample temperature.

5. Summary

Studies of oxygen adsorption and surface morphological instabilities induced by the presence of an oxygen overlayer on Ir(2 1 0) have been conducted. Oxygen is found to chemisorb dissociatively on Ir(2 1 0) at room temperature without oxide formation. The oxygen-covered Ir(2 1 0) forms pyramidal structures with {3 1 1} and (1 1 0) faces when annealed to 600 K and subsequently remains faceted for $T < 850$ K. For $T > 850$ K the structure reversibly transforms to the planar state. A clean faceted surface is prepared through the use of low temperature chemical cleaning methods (CO oxidation and reaction of H_2 to form H_2O). In this fashion oxygen can be removed from the surface while preserving ("freezing") the faceted structure. The clean faceted surface has been found to remain stable for $T < 600$ K. For $T > 600$ K this surface irreversibly relaxes to the planar state.

Appendix A

1. The high desorption temperatures measured in these experiments are consistent with a model in which oxygen molecules dissociate upon adsorption and the adsorbate consists entirely of atomic

oxygen. Such behavior has been observed in previous O/Ir adsorption experiments [35,36,51]. This, in conjunction with molecular oxygen desorption, indicates a second-order desorption process of the form $2O_{(ad)} \rightarrow O_{2(g)}$. Desorption can be modeled using the following differential equation:

$$R_d = -\frac{dn}{dt} = v_0^{(m)}(n)n^m \exp\left(-\frac{E_d(n)}{k_B T}\right), \qquad (A.1)$$

where R_d, n, t, $v_0^{(m)}(n)$, $E_d(n)$ and T are the desorption rate, adsorbate surface density, time, pre-exponential factor of the desorption rate coefficient, activation energy for desorption and sample temperature, respectively. The surface density dependencies of $v_0^{(m)}$ and E_d have been noted here for completeness, and because such dependencies have been observed in numerous adsorption/desorption experiments. To model a second-order process, a substitution $m = 2$ is made.

For low coverage ($D < 0.3$ L, corresponding to $\theta < 0.2$ ML) the TPD spectra bear a very close qualitative resemblance to second-order desorption curves: the peak (high temperature at ∼1300 K) is symmetric; [9] the peak temperature steadily decreases (Fig. 15) as dose/coverage increases and the curves for all coverages have a common trailing edge. However, upon closer inspection (Fig. 16) it becomes apparent that the peak width (FWHM) increases considerably with coverage (it almost doubles between 0.015 and 0.20 ML), whereas for a theoretical second-order desorption process at constant desorption energy, no such peak widening is present. With further coverage increase the spectra begin to differ noticeably from those predicted by the simple theoretical second-order model. For doses higher than 0.5 L a new feature (shoulder) develops on the low temperature side and gradually becomes an additional, lower temperature, peak with $900\ K < T_p < 830\ K$, depending on the dose. Once the dose exceeds 1.75 L, this peak becomes the dominant feature in the spectrum (Fig. 15 inset), indicating
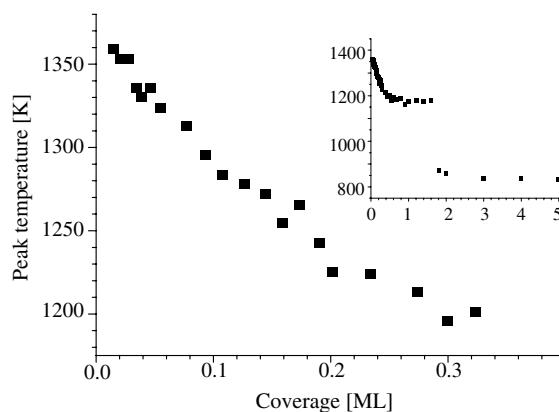

Fig. 15. Temperatures of TPD peaks as function of coverage for oxygen desorption from Ir(2 1 0).

the presence of two peaks associated with chemisorbed oxygen that have significantly different desorption activation energies, [10] similar to those observed for O/Ir(1 1 0) [35] and O/Ir(1 1 1) [36]. Results concerning the structure of the oxygen-covered surface (as described in Section 3.2) indicate that these two peaks do not necessarily originate from desorption from the (2 1 0) surface, but also from {3 1 1}, (1 1 0) and other orientations that appear at elevated temperatures, perhaps complicated by surface relaxation.

2. The differences observed in the peak shape between the experimentally obtained oxygen desorption spectra and ideal, second-order TPD spectra with unique and constant $v_0^{(m)}$ and E_d, are very small for the very lowest coverages. This considered, an attempt was made to treat these particular spectra as ideal ones and calculate the desorption parameters. The method described in [24] was initially used to calculate the activation energy E_d and pre-exponential coefficient $v_0^{(2)}$ for several spectra corresponding to these low doses (0.05–0.20 L, corresponding to 0.015–0.13 ML). A significant coverage dependence of the activation energy calculated in this way is immediately ob-

---

[9] The temperature of the peak of the desorption spectrum for the lowest dose in these experiments (0.05 L ⟺ 0.015 ML) is $T_p = 1350$ K.

[10] The contribution of the peak associated with a surface oxide layer is treated in the discussion section and is found to be sufficiently low to be negligible for the purpose of calculating the desorption parameters.
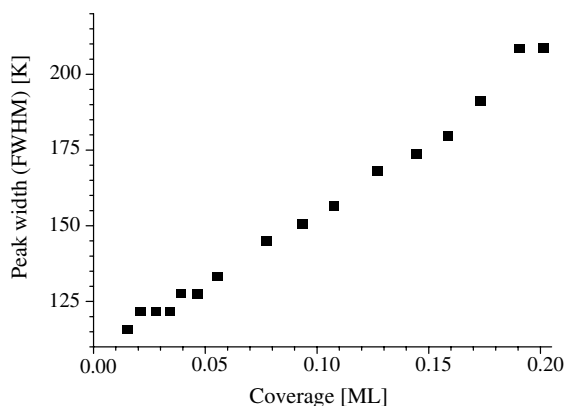
Fig. 16. Widths of TPD peaks as function of coverage for oxygen desorption from Ir(2 1 0).

served. For example, the desorption energy was found to be $E_d = 452$ kJ/mol for $\theta = 0.015$ ML, $E_d = 264$ kJ/mol for $\theta = 0.12$ ML. The calculations also yield values for $v_0^{(2)}$ that span a range of eight orders of magnitude. Attempts to fit all the low coverage spectra (for $\theta < 0.33$ ML), [11] assuming a simple second-order desorption process and using the parameters that give a satisfactory second-order fit for the lowest coverage ($\theta = 0.015$ ML), were completely unsuccessful. Little or no improvement in agreement was achieved by fitting each spectrum using the values for E_d and $v_0^{(2)}$ calculated for that particular spectrum. The differences between the experimentally obtained spectra and the calculated ones are apparent and become more pronounced as coverage increases, even in this narrow range of coverages.

3. In order to achieve better agreement with the experimental results, desorption curves were directly simulated using a first-principles approach, based on various choices for the values and the functional dependences of $v_0^{(2)}(\theta)$ and $E_d(\theta)$. To avoid complications due to the a priori unknown absolute oxygen surface density (e.g. oxygen atoms

per Ir(2 1 0) surface unit cell), all simulations were performed using the following dimensionless parameters [24]:

$$E^* = \frac{E_d}{RT^*} \quad \text{and} \quad v^{(2)} = \frac{v_0^{(2)} n_s T^*}{\beta}, \qquad (A.2)$$

where $R = 8.31$ J/mol/K is the gas constant and $T^* = 1$ K. It is only at the very end of the calculations that the reverse substitutions are made and $v_0^{(2)}(\theta)$ and $E_d(\theta)$ are obtained. The expected value of one oxygen atom per Ir(2 1 0) surface unit cell is substituted for the saturation coverage, in order to calculate $v_0^{(2)}$. For two atoms per unit cell the calculated values for $v_0^{(2)}$ would need to be divided by 2, etc.

Simulations based on a second-order process with adjusted, but still fixed parameters, yielded very little improvement. Somewhat better, but still unsatisfactory agreement was obtained by assuming a linear dependency of E_d on coverage ($E_d(\theta) = a + b\theta$). In order to obtain satisfactory agreement (Fig. 17) between experimental results and calculations in the whole coverage range considered (0.015–0.33 ML), it was found that a quadratic relation for $E_d(\theta)$ is required. Fitting with this approach yields
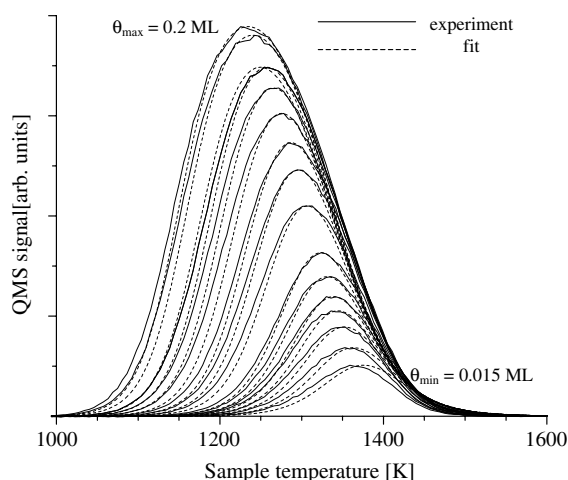
$$E^* = 54000 - 10000\theta - 50000\theta^2,$$

Fig. 17. Comparison between experimentally obtained TPD spectra and spectra calculated based on the model and parameters given in A.3.

---

[11] Coverage was considered "low" for this purpose, if the contribution of the low temperature peak to the spectrum was negligible. Generally, this was considered to be the case only for coverages that yielded a symmetric high-temperature peak.
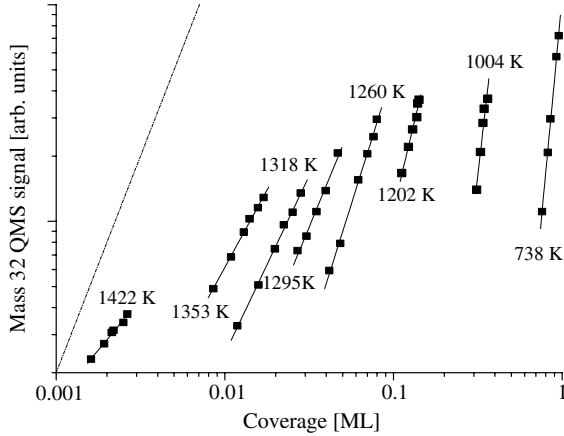
Fig. 18. Order plots for oxygen desorption from Ir(2 1 0). The slope of the fitted lines shows the apparent order of the desorption process and is equal to 2 (dotted line) for an ideal second-order process.

$v^{(2)} = 1.8^{18}$ for the dimensionless parameters.

This corresponds to

$$E_d = 4.66 - 0.86\theta - 4.31\theta^2 \ (eV/atom)$$
$$= 449 - 83.0\theta - 416\theta^2 \ (kJ/mol),$$

$$v_0^{(2)} = 0.149 \ m^2/s.$$

Further improvement in agreement was achieved by allowing $v_0^{(2)}$ to vary, and a more complicated functional dependence to exist for E_d. However, as shown below (see also Fig. 18) and explained in the discussion section, it is clear that the desorption process is inherently complex, and introducing further complicating details in the Arrhenius model that is used for these simulations, would lack a clear physical interpretation.

4. By rewriting (A.1) using $n = n_s\theta$ the desorption rate can be expressed as

$$R_d = -n_s \frac{d\theta}{dt}$$
$$= v_0^{(m)}(\theta)n_s^m\theta^m \exp\left(-\frac{E_d(\theta)}{k_B T_s}\right), \tag{A.3}$$

which, by plotting $\text{Log} \, R_d$ as a function of $\text{Log} \, \theta$, can be used to determine the order of the desorption process (m). If the desorption parameters $v_0^{(2)}(\theta)$ and $E_d(\theta)$ vary weakly within a coverage range, then the order, m, is given by the slope of this plot at points of constant temperature [25]. Since the pumping speed in the UHV system where the TPD measurements are performed is quite high, it is assumed that the desorption rate is proportional to the O_2 signal intensity, which is plotted instead. The coverage ranges for each temperature in Fig. 18 were conservatively chosen in order to minimize any discrepancies which may arise due to any coverage dependence of $v_0^{(2)}(\theta)$ and $E_d(\theta)$. The slopes of the lines fitted through the data vary approximately from a value of one, which occurs for very small coverages, to values exceeding eight as θ approaches unity (i.e. 1 ML). This is consistent with the strong coverage dependence that is exhibited by the activation energy E_d, and is a further indication of the difficulty faced in modeling the desorption kinetics for this system. Clearly, any values of obtained for $v_0^{(2)}$ and E_d can, at best, only be used to model the desorption process in a narrow range of oxygen coverage.

References

[1] J.C. Tracy, J.M. Blakely, Surf. Sci. 13 (1968) 313.
[2] R.E. Kirby, C.S. McKee, R.W. Roberts, Surf. Sci. 55 (1976) 725.
[3] R.E. Kirby, C.S. McKee, L.V. Renny, Surf. Sci. 97 (1980) 457.
[4] K.-J. Song, R.A. Demin, C. Dong, E. Garfunkel, T.E. Madey, Surf. Sci. Lett. 227 (1990) L79.
[5] K.-J. Song, C.-Z. Dong, T. Madey, Langmuir 7 (1991) 3019.
[6] K.-J. Song, J.C. Lin, M.Y. Lai, Y.L. Wang, Surf. Sci. 327 (1994) 17.
[7] M. Sander, R. Imbihl, R. Schuster, J.V. Barth, G. Ertl, Surf. Sci. 271 (1992) 159.
[8] S. Reiter, E. Taglauer, Surf. Sci. 367 (1996) 33.
[9] N. Reinecke, E. Taglauer, Surf. Sci. 454–456 (2000) 94.
[10] J.G. Che, C.T. Chan, C.H. Kuo, T.C. Leung, Phys. Rev. Lett. 79 (1997) 4230.
[11] M. Weinert, R.E. Watson, J.W. Davenport, G.W. Fernando, Phys. Rev. B 39 (1989) 12585.
[12] T.E. Madey, J. Guan, C.-H. Nien, C.-Z. Dong, H.-S. Tao, R.A. Campbell, Surf. Rev. Lett. 3 (1996) 1315.
[13] T.E. Madey, C.-H. Nien, K. Pelhos, J.J. Kolodziej, I.M. Abdelrehim, H.-S. Tao, Surf. Sci. 438 (1999) 191.
[14] F. Bonczek, T. Engel, E. Bauer, Surf. Sci. 97 (1980) 595.
[15] M.J. Gladys, G. Jackson, J.E. Rowe, T.E. Madey, Surf. Sci. 544 (2003) 193.

[16] C.-H. Nien, T.E. Madey, Y.W. Tai, T.C. Leung, J.G. Che, C.T. Chan, Phys. Rev. B 59 (1997) 10335.
[17] R.A. Campbell, J. Guan, T.E. Madey, Catal. Lett. 27 (1994) 273.
[18] R. Barnes, I.M. Abdelrehim, T.E. Madey, Topics Catal. 14 (2001) 53.
[19] J.J. Kolodziej, T.E. Madey, J.W. Keister, J.E. Rowe, Phys. Rev. B 65 (2002) 075413.
[20] M. Hansen, F.A. Shunk, Constitution of binary alloys, Second supplement, in: McGraw-Hill Series in Materials Science and Engineering, 1969, McGraw-Hill, New York, p. 461.
[21] M. Berday, S. Moldenhauer, A. Hammoudeh, J.H. Block, K. Christmann, Surf. Sci. 446 (2000) 323.
[22] P. Feulner, D. Menzel, Phys. Rev. B 25 (1982) 4295.
[23] C.T. Rettner, L.A. DeLouise, D.J. Auerbach, J. Chem. Phys. 85 (1986) 1131.
[24] C.-M. Chan, R. Aris, W.H. Weinberg, Appl. Surf. Sci. 1 (1978) 360.
[25] J.L. Falconer, R.J. Madix, J. Catal. 48 (1977) 262.
[26] H. Niehus, Surf. Sci. 87 (1979) 561.
[27] J. Guan, R.A. Campbell, T.E. Madey, Surf. Sci. 341 (1995) 311.
[28] K. Pelhos, I.M. Abdelrehim, C.-H. Nien, T.E. Madey, J. Phys. Chem. B 105 (2001) 3708.
[29] W. Chen, I. Ermanoski, T.E. Madey, in preparation.
[30] T.S. Wittrig, D.E. Ibbotson, W.H. Weinberg, Surf. Sci. 102 (1981) 506.
[31] W. Chen, I. Ermanoski, Q. Wu, T.E. Madey, H.H. Hwu, J.G. Chen, J. Phys. Chem. B 107 (2003) 5231.
[32] M.J. Gladys, I. Ermanoski, G. Jackson, J.S. Quinton, J.E. Rowe, T.E. Madey, J. Electron Spectros., submitted for publication.
[33] P. Kisliuk, J. Phys. Chem. Solids 5 (1958) 78.
[34] K. Pelhos, T.E. Madey, G.L. Kellog, J.B. Hannon, Surf. Rev. Lett. 6 (1999) 767.
[35] J.L. Taylor, D.E. Ibbotson, W.H. Weinberg, Surf. Sci. 79 (1979) 349.
[36] V.P. Ivanov, G.K. Boreskov, V.I. Savchenko, W.F. Egelhoff, W.H. Weinberg, Surf. Sci. 61 (1976) 207.
[37] C.Z. Dong, S.M. Shivaprasad, K.-J. Song, T.E. Madey, J. Chem. Phys. 99 (1993) 9172.
[38] J.M. Blakely, M. Eizenberg, in: D.A. King, D.P. Woodruff (Eds.), Morphology and Composition of Crystal Surfaces, The Chemical Physics of Solid Surfaces and Heterogeneous Catalysis, Elsevier Scientific Publishing Company, Amsterdam, Oxford, New York, 1981, p. 34.
[39] K. Pelhos, T.E. Madey, R. Blaszczyszyn, Surf. Sci. 426 (1999) 61.
[40] R. Kumar, H.E. Grenga, Surf. Sci. 50 (1975) 399.
[41] M.J. Kelly, Scr. Metal. Mater. 33 (1995) 1493.
[42] C. Chen, T.T. Tsong, Phys. Rev. Lett. 64 (1990) 3147.
[43] C.-L. Chen, T.T. Tsong, Phys. Rev. Lett. 66 (1991) 1610.
[44] S.S. Brenner, Surf. Sci. 2 (1964) 496.
[45] D. Spanjaard, M.C. Desjonquères, in: V. Bortolani, N.H. March, M.P. Tosi (Eds.), Electronic Theory of Chemisorption, Interaction of Atoms and Molecules with Solid Surfaces, Plenum Press, New York, London, 1990, p. 300.
[46] J.C. Heyraud, J.J. Métois, Surf. Sci. 128 (1983) 334.
[47] H.P. Bonzel, C.R. Helms, S. Kelemen, Phys. Rev. Lett. 35 (1975) 1237.
[48] T.N. Rhodin, G. Brodén, Surf. Sci. 60 (1976) 466.
[49] V.P. Zhdanov, B. Kasemo, Surf. Sci. 405 (1998) 27.
[50] S. Horch, H.T. Lorensen, S. Helveg, E. Lægsgaard, I. Stensgaard, K.W. Jacobsen, J.K. Nørskov, F. Besenbacher, Nature 398 (1999) 134.
[51] T. Ali, B. Klötzer, A.V. Walker, Q. Ge, D.A. King, J. Chem. Phys. 109 (1998) 9967.